ELECTROMAGNETIC SUBSURFACE DETECTION USING SUBSPACE SIGNAL PROCESSING AND HALF-SPACE DYADIC GREEN'S FUNCTION

X. F. Liu, B.-Z. Wang, and S. Q. Xiao

Institute of Applied Physics
University of Electronic Science and Technology of China
Chengdu, Sichuan 610054, China

Abstract—In this paper, one of the subspace signal processing methods, namely time reversal multiple signal classification (TR-MUSIC), is firstly employed for electromagnetic subsurface detection where the multilayered dyadic Green's function is used. Therewith, one obtains the improved location and superresolution imaging for underground detecting application. The imaging pseudo-spectrum is accordingly defined for both the echo-mode and transmit-mode TR-MUSIC methods, by analyzing the obtained multistatic response matrix. Based on the theoretical formula, we carry out the numerical simulation using the half-space dyadic Green's function in noisy scenario. The results show that the MUSIC imaging algorithm achieves the enhanced resolution and the transmit-mode method gives more robust output when performance comparison of the four methods is made, therefore indicate the TR-MUSIC could be a good candidate for subsurface detection.

1. INTRODUCTION

The time reversal imaging has been intensively studied in last two decades in both acoustics and electromagnetics due to the great potential application in many areas, such as nondestructive testing, wireless sensor network surveillance, target detection and reconnaissance. The mainly discussed imaging methods is chronologically listed as the iterative time reversal mirror imaging (ITRMI) [1–5], the decomposition of time reversal operator (DORT) [6–13] and the time reversal-multiple signal classification method (TR-MUSIC) [14–19]. The iterative time reversal mirror

---

Corresponding author: X. F. Liu (xfliu@uestc.edu.cn).

imaging is a most direct and intuitional method for target location and imaging considering the spatial and temporal focusing characteristics of time reversal mirror. However, since it uses the backpropagating wave to locate the scatters or targets, the resolution is still constrained to the Rayleigh criterion. Furthermore, the burden of iterative backpropagation and the difficulty in determining the focusing time arises. The DORT method uses the eigenvector in signal space of the multistatic response matrix to retrieve the target locations in an one-to-one manner. It evades the iterative process, therefore, releases the burden and improves the imaging efficiency. But when it comes to the cases with poorly resolved targets, i.e., two targets are so close that the distance between them is much smaller than half-wavelength, the DORT method encounters obstacle. To overcome this problem, the TR-MUSIC algorithm, which regards to the noise space of the multistatic response matrix or the time reversal marix, was proposed for superresolution imaging. It does not need wave backpropagation to locate the target and can image them at one time. The TR-MUSIC algorithm was firstly reported by *Devaney* [14–16] in the area of acoustic detection and imaging. Then it was quickly extended to the electromagnetic areas [17–19] due to the advantages on imaging quality and efficiency. However, most of the works were currently done in free space background media [23]. Actually in practice, many applications, both military and commercial, are in the scenarios with inhomogeneous background media, such as subsurface detection, through wall imaging and surveillance [24]. Therefore, it is beneficial to carry out the analysis and extend the method in this case. To do so, we employ the multilayered dyadic Green's function in constructing the time reversal matrix and performing MUSIC pseudo-spectrum for both transmit-mode and echo-mode configurations.

The TR-MUSIC algorithm is different from the original MUSIC method in statistical signal processing [20, 21]. The latter deals with the measured radar scattering data in the frequency-angular domain and then synthesize the covariance matrix from them to implement the location process, whereas the former starts from the multistatic response matrix between the transmit and receiver arrays. In this paper, we analyze the forward propagation and inverse scattering from the view of electromagnetic in detail to obtain the multistatic response matrix and time reversal matrix. Trough investigating the eigenvalue structure, it is observed that the so called signal space of the matrix is spanned by the background Green's function vectors evaluated at the target position. Upon that, the singular value decomposition of the time reversal matrix is performed so that the eigenvectors corresponding to the non-zero eigenvalues are in the signal space, and

the rest vectors are in the noise space which is orthogonal to the signal space. Based on this orthogonality, the MUSIC algorithm searches the imaging domain and locates the targets by checking the peak of the pseudo-spectrum at the position of the targets. Furthermore, we extended the algorithm to transmit-mode for two reasons. One is that the transmit-mode algorithm further increases the resolution and imaging quality due to its equivalent extended array aperture, and the second one is that it improves the capacity of detecting more targets and the flexibility of the algorithm.

The rest of this paper is organized as follows. In Section 2, the derivation of the time reversal matrix is discussed in detail. It is followed by the investigation of the eigenvalue structure and the MUSIC pseudospectrums are defined for both echo-mode and transmit-mode configurations. The performance analysis of the proposed algorithm is carried out using numerical simulation in Section 3, which validates the advantages of the proposed method. At last, Section 4 concludes the paper.

2. THEORY

In this section, the theoretical analysis is carried out to generate the multistatic response matrix and the time reversal matrix based on electromagnetic scattering theory and half-space dyadic Green's function.

2.1. The Forward Problem

We start with the model description of the detection system generally concerned. The transceiver array, not limited to be linear or planar, has M antenna elements located at $\mathbf{r}_m^t$, $m = 1, 2, \ldots, M$, which is usually on the earth's surface. Each of the elements consists of three dipole antennas oriented in the x, y and z direction with length l_{mx}, l_{my}, l_{mz} and driving current I_{mx}, I_{my}, I_{mz}, respectively. Therefore, the source at the mth element can be written as $\mathbf{J}_m = (I_{mx}l_{mx}\hat{x} + I_{my}l_{my}\hat{y} + I_{mz}l_{mz}\hat{z})\delta(\mathbf{r} - \mathbf{r}_m^t)$. The L scattering targets, which are assumed to be spheres with radius a_l, permittivity $\varepsilon(\mathbf{r}_l)$, and permeability $\mu(\mathbf{r}_l)$, respectively, are located at the underground positions $\mathbf{r}_l$, $l = 1, 2, \ldots, L$. Then incident electromagnetic fields at the location of the target $\mathbf{E}_{inc}^m(\mathbf{r}_l)$, $\mathbf{H}_{inc}^m(\mathbf{r}_l)$, excited by the mth source,

can be expressed as

$$\mathbf{E}_{inc}^m(\mathbf{r}_l) = i\omega\mu_0\left(\mathbf{r}_m^t\right)\overline{\overline{\mathbf{G}}}\left(\mathbf{r}_l, \mathbf{r}_m^t\right)\cdot\mathbf{J}_m, \tag{1}$$

$$\mathbf{H}_{inc}^m(\mathbf{r}_l) = \frac{\mu_0\left(\mathbf{r}_m^t\right)}{\mu_0(\mathbf{r}_l)}\nabla\times\overline{\overline{\mathbf{G}}}\left(\mathbf{r}_l, \mathbf{r}_m^t\right)\cdot\mathbf{J}_m. \tag{2}$$

where $\overline{\overline{\mathbf{G}}}$ is the multilayered dyadic Green's function which will be discussed in the following subsection, and $\mu_0(\mathbf{r})$ stands for the permeability of the background media at location $\mathbf{r}$. Considering all the antennas are excited at the same time, the incident fields upon the targets become the sum of M incident fields under the assumption that the multiple scattering between the targets is negligible. Writing in the matrix form, one can obtain

$$\overline{\mathbf{E}}_{inc} = \overline{\overline{P}}\cdot\overline{\overline{M}}\cdot\overline{\overline{L}}\cdot\overline{I}. \tag{3}$$

where

$$\overline{\mathbf{E}}_{inc} = \left[\mathbf{E}_{inc}^T(\mathbf{r}_1), \mathbf{E}_{inc}^T(\mathbf{r}_2), \ldots, \mathbf{E}_{inc}^T(\mathbf{r}_L),\right.$$
$$\left.\mathbf{H}_{inc}^T(\mathbf{r}_1), \mathbf{H}_{inc}^T(\mathbf{r}_2), \ldots, \mathbf{H}_{inc}^T(\mathbf{r}_L)\right]^T;$$
$$\overline{I} = [I_{1x}, I_{1y}, I_{1z}, I_{2x}, I_{2y}, I_{2z}, \ldots, I_{Mz}]^T;$$
$$\overline{\overline{L}} = \mathrm{diag}\left[l_{1x}, l_{1y}, l_{1z}, l_{2x}, l_{2y}, l_{2z}, \ldots, l_{Mz}\right];$$
$$\overline{\overline{M}} = \mathrm{diag}\left[\mu_0\left(\mathbf{r}_1^t\right), \mu_0\left(\mathbf{r}_1^t\right), \mu_0\left(\mathbf{r}_1^t\right), \mu_0\left(\mathbf{r}_2^t\right), \ldots, \mu_0\left(\mathbf{r}_M^t\right)\right];$$

and

$$\overline{\overline{P}} = \begin{bmatrix}\overline{\overline{\mathbf{G}}}^T \\ \overline{\overline{\mathbf{X}}}^T\end{bmatrix},$$

where $\overline{\overline{\mathbf{G}}}$ and $\overline{\overline{\mathbf{X}}}$ is shown as follows.

$$\overline{\overline{\mathbf{G}}} = \begin{bmatrix} i\omega\overline{\overline{\mathbf{G}}}\left(\mathbf{r}_1, \mathbf{r}_1^t\right), & i\omega\overline{\overline{\mathbf{G}}}\left(\mathbf{r}_2, \mathbf{r}_1^t\right), & \cdots & i\omega\overline{\overline{\mathbf{G}}}\left(\mathbf{r}_L, \mathbf{r}_1^t\right) \\ i\omega\overline{\overline{\mathbf{G}}}\left(\mathbf{r}_1, \mathbf{r}_2^t\right), & i\omega\overline{\overline{\mathbf{G}}}\left(\mathbf{r}_2, \mathbf{r}_2^t\right), & \cdots & i\omega\overline{\overline{\mathbf{G}}}\left(\mathbf{r}_L, \mathbf{r}_2^t\right) \\ \vdots & \vdots & \ddots & \vdots \\ i\omega\overline{\overline{\mathbf{G}}}\left(\mathbf{r}_1, \mathbf{r}_M^t\right), & i\omega\overline{\overline{\mathbf{G}}}\left(\mathbf{r}_2, \mathbf{r}_M^t\right), & \cdots & i\omega\overline{\overline{\mathbf{G}}}\left(\mathbf{r}_L, \mathbf{r}_M^t\right) \end{bmatrix};$$

$$\overline{\overline{\mathbf{X}}} = \begin{bmatrix} \frac{1}{\mu_0(\mathbf{r}_1)}\nabla \times \overline{\overline{\mathbf{G}}}\left(\mathbf{r}_1, \mathbf{r}_1^t\right), & \frac{1}{\mu_0(\mathbf{r}_2)}\nabla \times \overline{\overline{\mathbf{G}}}\left(\mathbf{r}_2, \mathbf{r}_1^t\right), \\ \frac{1}{\mu_0(\mathbf{r}_1)}\nabla \times \overline{\overline{\mathbf{G}}}\left(\mathbf{r}_1, \mathbf{r}_2^t\right), & \frac{1}{\mu_0(\mathbf{r}_2)}\nabla \times \overline{\overline{\mathbf{G}}}\left(\mathbf{r}_2, \mathbf{r}_2^t\right), \\ \vdots & \vdots \\ \frac{1}{\mu_0(\mathbf{r}_1)}\nabla \times \overline{\overline{\mathbf{G}}}\left(\mathbf{r}_1, \mathbf{r}_M^t\right), & \frac{1}{\mu_0(\mathbf{r}_2)}\nabla \times \overline{\overline{\mathbf{G}}}\left(\mathbf{r}_2, \mathbf{r}_M^t\right), \end{bmatrix}$$

$$\begin{matrix} \cdots & \frac{1}{\mu_0(\mathbf{r}_L)}\nabla \times \overline{\overline{\mathbf{G}}}\left(\mathbf{r}_L, \mathbf{r}_1^t\right) \\ \cdots & \frac{1}{\mu_0(\mathbf{r}_L)}\nabla \times \overline{\overline{\mathbf{G}}}\left(\mathbf{r}_L, \mathbf{r}_2^t\right) \\ \ddots & \vdots \\ \cdots & \frac{1}{\mu_0(\mathbf{r}_L)}\nabla \times \overline{\overline{\mathbf{G}}}\left(\mathbf{r}_L, \mathbf{r}_M^t\right) \end{matrix} \Bigg] ;$$

The scattering field, incident field and total field always hold the relationship as $\mathbf{E}_{tot}(\mathbf{r}_l) = \mathbf{E}_{inc}(\mathbf{r}_l) + \mathbf{E}_{sca}(\mathbf{r}_l)$. However, the Born approximation is usually employed for simplicity. It is valid when the contrast of the electrical or magnetic characteristics between the target and the background media is small. Here, we also adopt the Born approximation which implies that $\mathbf{E}_{tot}(\mathbf{r}_l) = \mathbf{E}_{inc}(\mathbf{r}_l)$, and it leads to the scattering field expressed as follows,

$$\mathbf{E}_{sca}\left(\mathbf{r}_m^t\right) = \sum_{l=1}^{L}\Bigg[4\pi a_l^3\omega^2\mu_0(\mathbf{r}_l)\varepsilon_0(\mathbf{r}_l)\frac{\varepsilon(\mathbf{r}_l)-\varepsilon_0(\mathbf{r}_l)}{\varepsilon(\mathbf{r}_l)+2\varepsilon_0(\mathbf{r}_l)}\cdot\overline{\overline{\mathbf{G}}}\left(\mathbf{r}_m^t, \mathbf{r}_l\right)\cdot\mathbf{E}_{inc}(\mathbf{r}_l)$$
$$-i4\pi a_l^3\omega^2\mu_0(\mathbf{r}_l)\cdot\frac{\mu(\mathbf{r}_l)-\mu_0(\mathbf{r}_l)}{\mu(\mathbf{r}_l)+2\mu_0(\mathbf{r}_l)}\nabla\times\overline{\overline{\mathbf{G}}}\left(\mathbf{r}_m^t, \mathbf{r}_l\right)\cdot\mathbf{H}_{inc}(\mathbf{r}_l)\Bigg] \tag{4}$$

It could be written in the matrix form,

$$\overline{\mathbf{E}}_{sca} = \left[\overline{\overline{\mathbf{G}}}, \overline{\overline{\mathbf{X}}}\right]\cdot\overline{\overline{F}}\cdot\overline{\mathbf{E}}_{inc} = \overline{\overline{Q}}\cdot\overline{\overline{F}}\cdot\overline{\mathbf{E}}_{inc} \tag{5}$$

where

$$\overline{\overline{F}} = \text{diag}\left[\overline{\overline{F}}_\varepsilon, \overline{\overline{F}}_\mu\right];$$
$$\overline{\overline{F}}_\varepsilon = \text{diag}\left[\overline{\overline{\xi}}_1, \overline{\overline{\xi}}_2, \ldots, \overline{\overline{\xi}}_L\right];$$
$$\overline{\overline{F}}_\mu = \text{diag}\left[\overline{\overline{\zeta}}_1, \overline{\overline{\zeta}}_2, \ldots, \overline{\overline{\zeta}}_L\right];$$
$$\overline{\overline{\xi}}_l = -4\pi a_l^3\omega^2\mu_0(\mathbf{r}_l)\varepsilon_0(\mathbf{r}_l)\frac{\varepsilon(\mathbf{r}_l)-\varepsilon_0(\mathbf{r}_l)}{\varepsilon(\mathbf{r}_l)+2\varepsilon_0(\mathbf{r}_l)}\cdot\mathbf{I}_3;$$
$$\overline{\overline{\zeta}}_l = -i4\pi a_l^3\omega^2\mu_0(\mathbf{r}_l)\frac{\mu(\mathbf{r}_l)-\mu_0(\mathbf{r}_l)}{\mu(\mathbf{r}_l)+2\mu_0(\mathbf{r}_l)}\cdot\mathbf{I}_3.$$

and $\mathbf{I}_3$ denotes identity matrix with size 3×3. The analysis is easy to extended to the cases with anisotropic targets by replacing $\overline{\overline{\xi}}_l$ and

$\overline{\overline{\zeta}}_l$ with the electric and magnetic polarization strength tensors of the targets and modifying the matrix $\overline{\overline{M}}$.

Then, the voltages induced on the antenna dipoles can be obtained in a vector form defined as: $\overline{V} = [V_{1x}, V_{1y}, V_{1z}, V_{2x}, V_{2y}, V_{2z}, \ldots, V_{Mz}]^T$. One arrives at,

$$\overline{V} = \overline{\overline{L}} \cdot \overline{\mathbf{E}}_{sca}. \tag{6}$$

Combining the Eqs. (1), (5), (6), the expression of the transfer function could be achieved and the so call multistatic response matrix is represented as

$$\overline{\overline{K}} = \overline{\overline{L}} \cdot \overline{\overline{Q}} \cdot \overline{\overline{F}} \cdot \overline{\overline{P}} \cdot \overline{\overline{M}} \cdot \overline{\overline{L}}. \tag{7}$$

Furthermore, the time reversal matrix is

$$\overline{\overline{T}} = \overline{\overline{K}}^* \cdot \overline{\overline{K}}. \tag{8}$$

where $*$ denotes the conjugate transpose.

2.2. The TR-MUSIC Algorithm

It has already been mentioned that the DORT imaging can be performed using the back-propagation of the singular vectors associated to nonzero singular values of the time reversal matrix [6, 7]. But it requires that the targets are well-separated, which means that they are not sufficiently separated from each other. Furthermore, the DORT method can only locate individual target with one back-propagation of one set of singular vector in acoustic applications. But in electromagnetic application, the relationship become more complex due to polarization, array configuration, shape and electromagnetic characteristics of the targets, and so on. Therefore the TR-MUSIC algorithm is proposed and expected to become our possible solution to this problem. There is a little similarity to the DORT method in the derivation because it is also based on the singular value decomposition of the $\overline{\overline{K}}$ matrix, which has the so called signal subspace $\mathcal{S}_s$ spanned by the background Green's function vectors evaluated at the target locations. The singular system is given as follows,

$$\begin{aligned} \overline{\overline{K}} u_j &= \sigma_j v_j, \\ \overline{\overline{K}}^* v_j &= \sigma_j u_j. \end{aligned} \tag{9}$$

where σ_j, u_j, and v_j are the jth singular value and the jth column vector of the orthonormal matrices U and V^*, respectively. Then we can draw that the range space of the $\overline{\overline{K}}$ matrix is divided into signal space $\mathcal{S}_s$ and noise space $\mathcal{S}_n$. They are orthogonal and, respectively,

spanned by the singular vector v_j corresponding to nonzero singular values and zero singular values, i.e., $\mathcal{S}_s = Span\{v_j, \sigma_j > 0\} \perp \mathcal{S}_n = Span\{v_j, \sigma_j = 0\}$. By observing the relationship between the background Green's function vectors and the singular vectors, it comes to the equation

$$v_j^* \overline{\mathbf{G}}_i(\mathbf{r}_l) = v_j^* \overline{\mathbf{X}}_i(\mathbf{r}_l) = 0, \quad \text{for} \quad \sigma_j = 0. \tag{10}$$

where $l = 1, 2, \ldots, L$, $i = 1, 2, 3$, and

$$\overline{\mathbf{G}}(\mathbf{r}) = \begin{bmatrix} i\omega\overline{\overline{\mathbf{G}}}\left(\mathbf{r}, \mathbf{r}_1^t\right) \\ i\omega\overline{\overline{\mathbf{G}}}\left(\mathbf{r}, \mathbf{r}_2^t\right) \\ \vdots \\ i\omega\overline{\overline{\mathbf{G}}}\left(\mathbf{r}, \mathbf{r}_M^t\right) \end{bmatrix}, \quad \overline{\mathbf{X}}(\mathbf{r}) = \begin{bmatrix} \frac{1}{\mu_0(\mathbf{r})}\nabla \times \overline{\overline{\mathbf{G}}}\left(\mathbf{r}, \mathbf{r}_1^t\right) \\ \frac{1}{\mu_0(\mathbf{r})}\nabla \times \overline{\overline{\mathbf{G}}}\left(\mathbf{r}, \mathbf{r}_2^t\right) \\ \vdots \\ \frac{1}{\mu_0(\mathbf{r})}\nabla \times \overline{\overline{\mathbf{G}}}\left(\mathbf{r}, \mathbf{r}_M^t\right) \end{bmatrix},$$

and the subscript i denotes the ith column of $\overline{\mathbf{G}}(\mathbf{r})$ and $\overline{\mathbf{X}}(\mathbf{r})$, which are both $3M \times 3$ matrices. Consequently, following the previous reports [13–15], the TR-MUSIC pseudo-spectrum is defined as

$$P_{em}(\mathbf{r}) = 1 / \sum_{\sigma_j=0} \left[\sum_{i=1,2,3} \left| v_j^* \overline{\mathbf{G}}_i(\mathbf{r}) \right|^2 + \sum_{i=1,2,3} \left| v_j^* \overline{\mathbf{X}}_i(\mathbf{r}) \right|^2 \right] \tag{11}$$

In the above, the algorithm scans the imaging domain by $\mathbf{r}$, and the pseudo-spectrum becomes infinite at the target positions $\mathbf{r}_l, l = 1, 2, \ldots, L$. It is notable that, to locate all the targets, $3M$ must be large than the six times of the number of the targets since one target can be associated to at most six nonzero singular values [9, 12, 13], so that the multistatic response matrix exists zero singular values to perform the TR-MUSIC searching in theory. However, in practice, the system requires more antenna elements to achieve good performance due to the loss and noise, and so on.

2.3. Transmit-mode Analysis

The previous discussion is all based on the echo-mode transceiver structure. In fact, many applications prefer the transmit-mode transceiver, such as bore-hole tomography, distributed sensing and imaging. In addition, extending the study to transmit-mode also brings some extra improvements, which include bringing more accurate location and higher resolution imaging because the noncoincident arrays actually increase the effectual aperture of the array and making the algorithm more flexible and practical. To analyze the transmit-mode, we modify the previously discussed echo-mode model with

adding a receiver array, which has N antenna elements located at $\mathbf{r}_n^r$, $n = 1, 2, \ldots, N$. Also each element consists of three dipole antennas oriented in the x, y and z direction with length l'_{nx}, l'_{ny}, l'_{nz}, respectively.

Accordingly, in this case Eq. (4) is changed by replacing $\mathbf{r}_m^t$ with $\mathbf{r}_n^r$. It is followed by

$$\overline{\mathbf{E}}'_{sca} = \left[\overline{\overline{\mathbf{G}'}}, \overline{\overline{\mathbf{X}'}}\right] \cdot \overline{\overline{F}} \cdot \mathbf{E}_{inc} = \overline{\overline{Q'}} \cdot \overline{\overline{F}} \cdot \mathbf{E}_{inc} \tag{12}$$

where $\overline{\overline{\mathbf{G}'}}$ and $\overline{\overline{\mathbf{X}'}}$ are $3N \times 3L$ matrices obtained also by replacing $\mathbf{r}_m^t$ with $\mathbf{r}_n^r$. Then, similarly, one has the multistatic response matrix $\overline{\overline{\mathbf{K}'}}$ as

$$\overline{\overline{K'}} = \overline{\overline{L'}} \cdot \overline{\overline{Q'}} \cdot \overline{\overline{F}} \cdot \overline{\overline{P}} \cdot \overline{\overline{M}} \cdot \overline{\overline{L}}, \tag{13}$$

where $\overline{\overline{L'}} = \mathrm{diag}[l'_{1x}, l'_{1y}, l'_{1z}, l'_{2x}, l'_{2y}, l'_{2z}, \ldots, l'_{Nz}]$. Here $\overline{\overline{K'}}$ is a $3N \times 3M$ matrix which represents a mapping from the transmitter to receiver space and its Hermitian, $\overline{\overline{K'}}^*$, represents a mapping from the receiver to transmitter space. Consequently, the so called transmitter and receiver time reversal matrices $\overline{\overline{T}}_t = \overline{\overline{K'}}^* \overline{\overline{K'}}$ and $\overline{\overline{T}}_r = \overline{\overline{K'K'}}^*$ have the singular system as

$$\begin{aligned} \overline{\overline{T}}_t u_j &= \sigma_j^2 u_j, \\ \overline{\overline{T}}_r v_j &= \sigma_j^2 v_j. \end{aligned} \tag{14}$$

The transmitter and receiver spaces are spanned by u_j and v_j, respectively. They can be both subdivided into signal space and noise space, which is spanned by the singular vectors corresponding to nonzero singular values and zero singular values, respectively. The relationship can be expressed as

$$\begin{aligned} \mathcal{S}^t &= \mathcal{S}_s^t \oplus \mathcal{S}_n^t, \ \ \mathcal{S}^r = \mathcal{S}_s^r \oplus \mathcal{S}_n^r, \\ \mathcal{S}_s^t &= Span\{u_j, \sigma_j > 0\} \perp \mathcal{S}_n^t = Span\{u_j, \sigma_j = 0\}, \\ \mathcal{S}_s^r &= Span\{v_j, \sigma_j > 0\} \perp \mathcal{S}_n^r = Span\{v_j, \sigma_j = 0\} \end{aligned}$$

On the other hand, the background media Green's function vectors are the orthonormal bases of the signal space. Therefore, the inner product of the background Green's function vectors of the target locations and singular vectors in noise space theoretically equals to zero. One obtains

$$\begin{aligned} u_j^* \overline{\mathbf{G}}_i(\mathbf{r}_l) &= u_j^* \overline{\mathbf{X}}_i(\mathbf{r}_l) = 0, \quad \text{for } \sigma_j = 0; \\ v_j^T \overline{\mathbf{G}'}_i(\mathbf{r}_l) &= v_j^T \overline{\mathbf{X}'}_i(\mathbf{r}_l) = 0, \quad \text{for } \sigma_j = 0. \end{aligned} \tag{15}$$

where $i = 1, 2, 3$; $l = 1, 2, \ldots, L$; $\overline{\mathbf{G}}_i(\mathbf{r}_l)$ and $\overline{\mathbf{X}}_i(\mathbf{r}_l)$ are the same as previously defined ones; $\overline{\mathbf{G}'}_i(\mathbf{r}_l)$ and $\overline{\mathbf{X}'}_i(\mathbf{r}_l)$ are given by first

substituting $\mathbf{r}_n^r$ for $\mathbf{r}_m^t$ in $\overline{\mathbf{G}}_i(\mathbf{r}_l)$ and $\overline{\mathbf{X}}_i(\mathbf{r}_l)$, then exchanging the positions of $\mathbf{r}$ and $\mathbf{r}_n^r$. Now, one defines the pseudo-spectrum $P_{tm}(\mathbf{r})$ of the transmit-mode TR-MUSIC algorithm to be

$$
\begin{aligned}
P_{tm}(\mathbf{r}) \;=\; 1/ \sum_{\sigma_j=0} &\left[\sum_{i=1,2,3} \left| v_j^* \overline{\mathbf{G}}_i(\mathbf{r}) \right|^2 + \sum_{i=1,2,3} \left| v_j^* \overline{\mathbf{X}}_i(\mathbf{r}) \right|^2 \right. \\
&\left. + \sum_{i=1,2,3} \left| u_j^T \overline{\mathbf{G}'}_i(\mathbf{r}) \right|^2 + \sum_{i=1,2,3} \left| u_j^T \overline{\mathbf{X}'}_i(\mathbf{r}) \right|^2 \right]
\end{aligned}
\tag{16}
$$

2.4. Computation of Dyadic Green's Function

The computation of the multilayered dyadic Green's function employed here follows the way described in [22]. Considering the highlighted application to subsurface detection, one observes it in a model setup with two layered planar media that denotes the upper half-space and lower half-space. In this case, for an observation point $\mathbf{r}$ at one half-space away from the source point $\mathbf{r}'$ at the opposite half-space, the dyadic Green's function is given by

$$
\overline{\overline{\mathbf{G}}}(\mathbf{r},\mathbf{r}') = \frac{i}{8\pi^2} \iint\limits_{-\infty}^{+\infty} \frac{d\mathbf{k_s}}{k_{+,z}k_s^2} \left[\overline{\overline{\mathbf{M}}}\left(\mathbf{k}_s,\mathbf{r},\mathbf{r}'\right) + \overline{\overline{\mathbf{N}}}\left(\mathbf{k}_s,\mathbf{r},\mathbf{r}'\right) \right] - \frac{\hat{z}\hat{z}}{k_+^2}\delta\left(\mathbf{r},\mathbf{r}'\right) \tag{17}
$$

where

$$
\begin{aligned}
\overline{\overline{\mathbf{M}}}(\mathbf{k}_s,\mathbf{r},\mathbf{r}') &= (\nabla \times \hat{z})(\nabla' \times \hat{z}) e^{i\mathbf{k}_s \cdot (\mathbf{r}_s - \mathbf{r}'_s)} F^{\mathrm{TE}}(z,z'), \\
\overline{\overline{\mathbf{N}}}(\mathbf{k}_s,\mathbf{r},\mathbf{r}') &= \left(\frac{\nabla \times \nabla \times \hat{z}}{i\omega\varepsilon_-} \right)\left(\frac{\nabla' \times \nabla' \times \hat{z}}{-i\omega\mu_+} \right) e^{i\mathbf{k}_s \cdot (\mathbf{r}_s - \mathbf{r}'_s)} F^{\mathrm{TM}}(z,z'), \\
F^{\mathrm{TE,TM}}(z,z') &= e^{-ik_{-,z}(z+d_1)} T^{\mathrm{TE,TM}} e^{-ik_{+,z}(d_1-z')}, \\
T^{\mathrm{TE}} &= \frac{2\mu_- k_{+,z}}{\mu_- k_{+,z} + \mu_+ k_{-,z}}, \\
T^{\mathrm{TM}} &= \frac{2\varepsilon_- k_{+,z}}{\varepsilon_- k_{+,z} + \varepsilon_+ k_{-,z}},
\end{aligned}
$$

here, the subscripts $+$ and $-$ label the parameters of the half-spaces where the source point and observation point locate, respectively; $\mathbf{k}_s = \hat{x}k_x + \hat{y}k_y$; $\mathbf{r}_s = \hat{x}x + \hat{y}y$; d_1 is z axis of the interface between the two half-spaces. It is notable that the Green's function satisfies the reciprocity $\overline{\overline{\mathbf{G}}}(\mathbf{r},\mathbf{r}')\mu(\mathbf{r}') = \overline{\overline{\mathbf{G}}}^T(\mathbf{r}',\mathbf{r})\mu(\mathbf{r})$, which can reduce the computation cost. However, since the emphasis is on the TR-MUSIC and its application, we would not attempt to use any fast-algorithm to compute the Green's function.

3. PERFORMANCE INVESTIGATION

In this section, we carry out two numerical examples to verify the feasibility and the improved imaging resolution of the proposed TR-MUSIC algorithm in the applications of underground detection. They are carried out in this way: First, the K matrix is obtained by using Eq. (7); then the obtained K matrix is contaminated with the additive white Gaussian noise; At last, the echo-mode and transmit-mode algorithms based on Eqs. (11) and (16) are used to locate the targets and image the concerned domain. We first describe the detection system model as shown in Fig. 1. The dash rectangle is the plane $z = d_1 = -4$ which denotes the interface between the air and subsurface. The transmitter array and the receiver array locate at the plane $z = 0$, which are both set to be planar array. When the detection and imaging system works in the echo-mode, the array is monostatic. Comparatively, the elements of the array are divided into two group in transmit-mode, which work independently to realize the bistatic mechanism. The spheral targets are buried underground and located in a limited three dimensional imaging domain. In this representation, the targets are assumed to be relatively small comparing with the operating wavelength as discussed in the previous theoretical derivation. However, an approximate approach for the extended targets detection is to discrete the targets into a set of small spheres and then perform the TR-MUSIC algorithm.

3.1. 3D Evaluation

In this subsection, one performs the three dimensional detection of underground targets based on the numerical experiment. The system is described as follows. The 16 transmitter elements and 16 receiver elements of the arrays are all arranged in the xoy ($z = 0$) plane. The
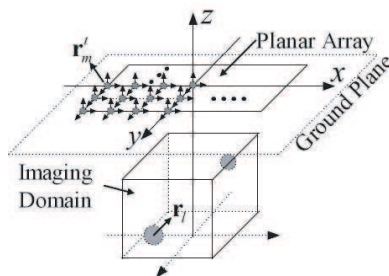
Figure 1. The configuration of the concerned detection model.

transmitter array is placed in a cross shape with an element distance of 5λ. Meanwhile, the receiver array is arranged in the same way except that it is moved 40λ away form the transmitter array in x direction. In the echo-mode simulations, only the transmitter array works in a monostatic way. And in the transmit-mode ones, both the transmitter and receiver arrays work. The available imaging domain is a 3D box with a size of $6\lambda \times 6\lambda \times 6\lambda$ as shown in Fig. 1. The spherical scatterer is placed at the center of the imaging box and have a radius of $a_1 = \lambda/15$ and a distance of 10λ from the center of the transmitter array. The underground electromagnetic parameters are $\varepsilon_0(\mathbf{r}) = 2\varepsilon_0$, $\mu_0(\mathbf{r}) = 1.5\mu_0$ and the electromagnetic parameters of the scatterer are $\varepsilon(\mathbf{r}_1) = 3.5\varepsilon_0$, $\mu(\mathbf{r}_1) = 2.5\mu_0$. The frequency of the system is chosen at $100\,\mathrm{MHz}$. To evaluate the performance in a more practical way, we consider that the transfer matrix $\overline{\overline{K}}$ is contaminated with the additive white Gaussian noise. The noise level is also controlled by the signal-noise-ratio which is defined in [18] as $20\log_{10}(\|\overline{\overline{K}}\|/\|\overline{\overline{k}}\|)$, where $\|\overline{\overline{k}}\|$ is the additive white Gaussian noise. Figs. 2 and 3 show the three dimensional imaging results of the buried target for echo-mode and transmit-mode TR MUSIC algorithms, respectively. The

(a) SNR = -10 dB

(b) SNR = 10 dB
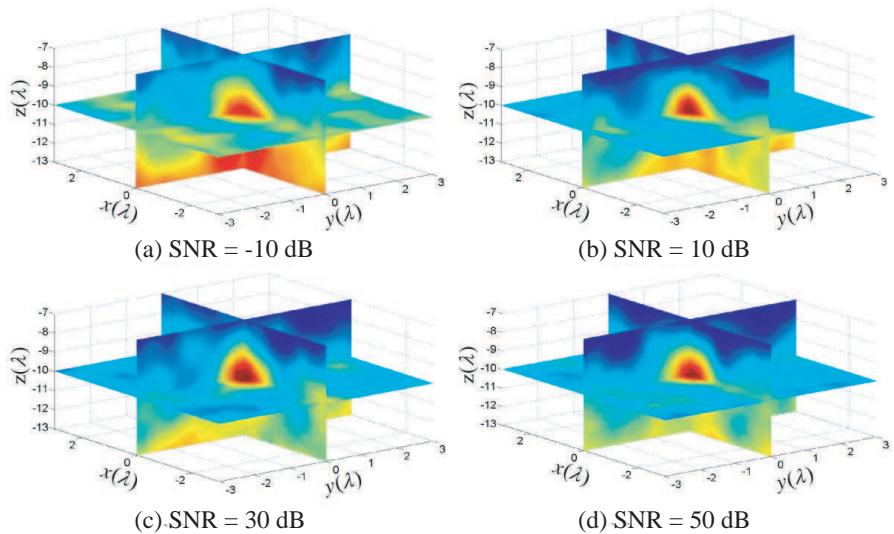
(c) SNR = 30 dB

(d) SNR = 50 dB

Figure 2. The 3D imaging results of the echo-mode TR MUSIC algorithm (P_{em}) with operation frequency $f = 100\,\mathrm{MHz}$ and different signal-noise-ratios: (a) SNR $= -10\,\mathrm{dB}$, (b) SNR $= 10\,\mathrm{dB}$, (c) SNR $= 30\,\mathrm{dB}$, (d) SNR $= 50\,\mathrm{dB}$. The target is located at $(0, 0, -10\lambda)$.

(a) SNR = -10 dB

(b) SNR = 10 dB
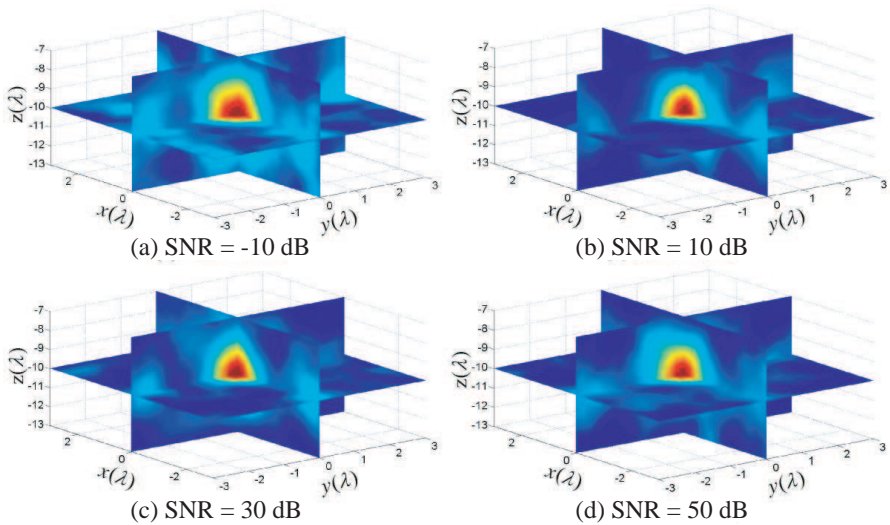
(c) SNR = 30 dB

(d) SNR = 50 dB

Figure 3. The 3D imaging results of the transmit-mode TR MUSIC algorithm (P_{tm}) with operation frequency $f = 100$ MHz and different signal-noise-ratios: (a) SNR $= -10$ dB, (b) SNR $= 10$ dB, (c) SNR $= 30$ dB, (d) SNR $= 50$ dB. The target is located at $(0, 0, -10\lambda)$.

signal-noise-ratio is chosen to be -10 dB, 10 dB, 30 dB and 50 dB. It is obviously presented that both the echo-mode and transmit-mode can well and truly locate the target even when the signal-noise-ratio is very low. However, the latter provides better resolution and shaper imaging as shown in Fig. 3. And it also can be observed that the transmit-mode is much more robust against the increase of the noise than the echo-mode. These advantages appear due to the increased array aperture of the transmit-mode method. In addition, one can tell from the configuration of the transmit-mode that more flexible and practical systems can be achieved for many potential application, such as underwater detection and imaging, distributed surveillance and so on.

3.2. Performance Comparison

In this second numerical investigation, one compares the 3D imaging of these primary time reversal imaging methods (echo-mode and transmit-mode DORT) with the proposed methods (echo-mode and transmit-mode TR MUSIC). The setup of the simulation model is the same as the model in the last subsection except that the receiver array

(a) Echo-mode DORT

(b) Transmit-mode DORT

(c) Echo-mode DORT

(d) Transmit-mode TR MUSIC
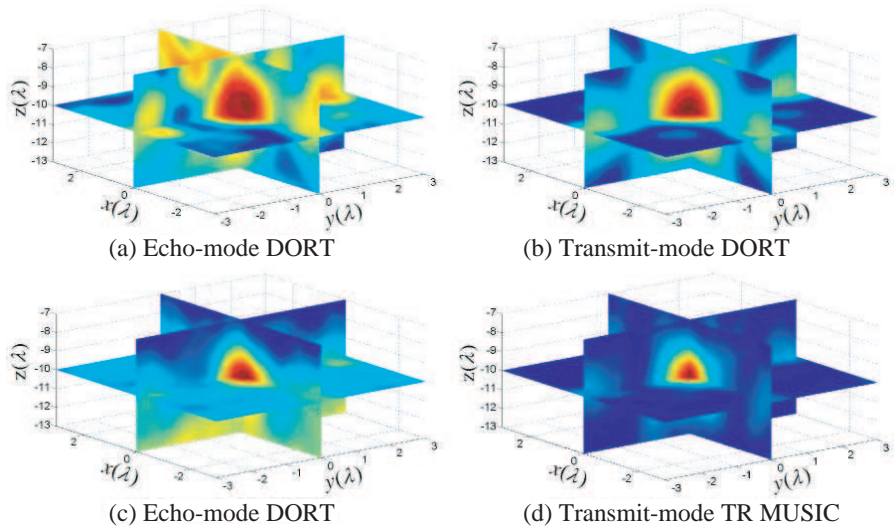
Figure 4. The 3D imaging results of one target, located at $(0, 0, -10\lambda)$, by using the four method: (a) Echo-mode DORT, (b) Transmit-mode DORT, (c) Echo-mode TR MUSIC (P_{em}), (d) Transmit-mode TR MUSIC (P_{tm}). The operation frequency is $f = 100\,\mathrm{MHz}$ and the signal-noise-ratios is set to be SNR = 20 dB.
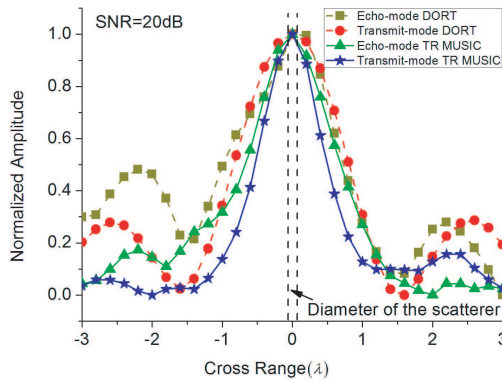
Figure 5. The normalized amplitude of the pseudospectrum in the cross range of the imaging results for four algorithms: The echo-mode DORT, the transmit-mode DORT, the echo-mode TR MUSIC (P_{em}) and the transmit-mode TR MUSIC (P_{tm}) when SNR = 20 dB, $f = 100\,\mathrm{MHz}$.

is changed to be placed at the $z = -20\lambda$ plane. The centers of the transmitter array, the imaging box and the receiver array are colinear: $(0, 0, 0)$, $(0, 0, -10\lambda)$ and $(0, 0, -20\lambda)$. This alteration can further improve the imaging resolution especially for the scenarios with far field detection.

When the operation frequency is set to be 100 MHz, and the signal-noise-ratio is 20 dB, the 3D imaging results of one scatterer located at the center $(0, 0, -10\lambda)$ of the imaging box, using these four time reversal imaging methods, are obtained as shown in Fig. 4. It could be seen that the proposed TR MUSIC algorithms, both echo-mode and transmit-mode, have shaper imaging result that the conventional DORT algorithm. Agreeing with the expectance, the transmit-mode methods are of the better performance than the echo-mode methods since they actually have the increased effective array aperture. If one draw the normalized amplitude of the pseudospectrums on a one-dimensional cross range $(y = 0, z = -10\lambda)$, one can observe the above conclusions more clearly as depicted in Fig. 5. The distance between the two dash upright lines denotes the diameter of the

(a) Echo-mode DORT

(b) Transmit-mode DORT

(c) Echo-mode DORT

(d) Transmit-mode TR MUSIC
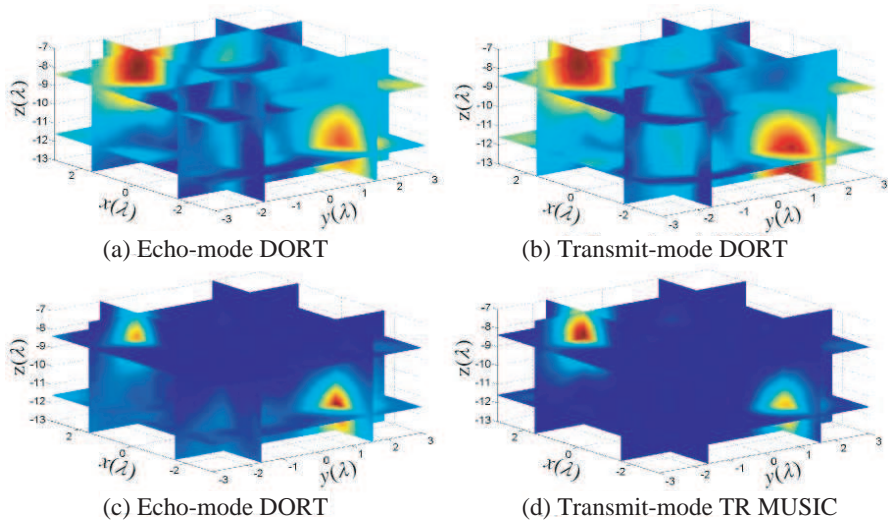
Figure 6. The 3D imaging results of two targets, located at $(1.67\lambda, -1.67\lambda, -8.33\lambda)$ and $(-1.67\lambda, 1.67\lambda, -11.67\lambda)$, by using the four method: (a) Echo-mode DORT, (b) Transmit-mode DORT, (c) Echo-mode TR MUSIC (P_{em}), (d) Transmit-mode TR MUSIC (P_{tm}). The operation frequency is $f = 100$ MHz and the signal-noise-ratios is set to be SNR $= 20$ dB.

target. Obviously from the blue curve, the transmit-mode TR MUSIC algorithm is proved having closest pseudospectrum distribution to the actual target and having restrained sidelobe of the pseudospectrum.

Figure 6 presents the example of detecting two scatterers by using these four time reversal imaging methods. It could be seen that the DORT method would be difficult to distinguish multiple targets when the distance among the targets is relatively small. Comparatively, the TR MUSIC methods can combat this obstacle more effectively because of the improved resolution. This is a valuable improvement in the concerned underground detection, because when one comes with extended targets, this enhancement is beneficial to profiling the targets.

The examples are investigated in rather an academic situation in this paper, however it verifies that the proposed TR MUSIC method combined with the half-space Green's function is a very promising detection algorithm comparing with the former DORT method, mainly due to the improvement on the imaging resolution.

4. CONCLUSION

In this paper, we investigate the time reversal MUSIC algorithm for detection and imaging of the subsurface targets, by introducing the half-space dyadic Green's function. The theoretical derivation of the time reversal matrix is first discussed in detail when the assumption that the BORN approximation is valid for the model is made. Then, according to the antenna array configurations, the echo-mode and transmit-mode pseudospectrums are defined. This provides more options for the practical applications in different situations, such as subsurface detection, underwater surveillance and medical imaging etc. The numerical examples verify the feasibility and flexibility of the proposed method. Furthermore, the comparison between the conventional DORT methods and the proposed methods is performed, which proves that the TR MUSIC methods have better robustness and give higher resolution of the imaging. Therefore, one concludes that the proposed method is an effective solution of subsurface detection and a promising candidate of high quality imaging.

ACKNOWLEDGMENT

REFERENCES

1. Fink, M., "Time reversal mirrors," *J. Phys. D: Appl. Phys.*, Vol. 26, 1333–1350, 1993.

2. Prada, C., J. L. Thomas, and M. Fink, "The iterative time reversal process: Analysis of the convergence," *J. Acoust. Soc. Am.*, Vol. 97, 62–71, 1995.

3. Kuperman, W. A., W. S. Hodgkiss, H. C. Song, T. Akal, C. Ferla, and D. R. Jackson, "Phase conjugation in the ocean: Experimental demonstration of an acoustic time reversal mirror," *J. Acoust. Soc. Am.*, Vol. 103, 25–40, 1998.

4. Zheng, W., Z. Zhao, and Z.-P. Nie, "Application of TRM in the UWB through wall radar," *Progress In Electromagnetics Research*, PIER 87, 279–296, 2008.

5. Zheng, W., Z. Zhao, Z.-P. Nie, and Q. H. Liu, "Evaluation of TRM in the complex through wall environment," *Progress In Electromagnetics Research*, PIER 90, 235–254. 2009.

6. Prada, C., S. Manneville, D. Spoliansky, and M. Fink, "Decomposition ofthe time reversal operator: Detection and selective focusing on two scatterers," *J. Acoust. Soc. Am.*, Vol. 99, 2067–2076, 1996.

7. Folegot, T., C. Prada, and M. Fink, "Resolution enhancement and separation of reverberation from target echo with the time reversal operator decomposition," *J. Acoust. Soc. Am.*, Vol. 113, 3155–5160, 2003.

8. Tortel, H., G. Micolau, and M. Saillard, "Decomposition of the time reversal operator for electromagnetic scattering," *Journal of Electromagnetic Waves and Applications*, Vol. 13, No. 5, 687–719, 1999.

9. Chambers, D. and A. Gautesen, "Time reversal for a single spherical scatter," *J. Acoust. Soc. Am.*, Vol. 109, 2616–2624, 2001.

10. Mordant, N., C. Prada, and M. Fink, "Highly resolved detection and selective focusing in a waveguide using the D.O.R.T. method," *J. Acoust. Soc. Am.*, Vol. 105, 2634–2642, 1999.

11. Gaumond, C. F., D. M. Fromm, J. F. Lingevitch, R. Menis, G. F. Edelmann, D. C. Calvo, and E. Kim, "Demonstration at sea of the decomposition-of-the-time-reversal-operator technique," *J. Acoust. Soc. Am.*, Vol. 119, 976–990, 2006.

12. Rao, T. and X. Chen, "Analysis of the time-reversal operator fora single cylinder under two-dimensional settings," *Journal of Electromagnetic Waves and Applications*, Vol. 20, No. 15, 2153–2165, 2006.

13. Chen, X., "Time-reversal operator for a small sphere in electromagnetic fields," *Journal of Electromagnetic Waves and Applications*, Vol. 21, No. 9, 1219–1230, 2007.

14. Devaney, A. J., "Time reversal imaging of obscured targets from multistatic data," *IEEE Trans. Antennas & Propag.*, Vol. 53, 1600–1610, 2005.

15. Devaney, A. J., E. A. Marengo, and F. K. Gruber, "Time-reversal-based imaging and inverse scattering of multiply scattering point targets," *J. Acoust. Soc. Am.*, Vol. 115, 3129–3138, 2005.

16. Gruber, F. K., E. A. Marengo, and A. J. Devaney, "Time-reversal imaging with multiple signal classification considering multiple scattering between the targets," *J. Acoust. Soc. Am.*, Vol. 115, 3042–3047, 2004.

17. Ammari, H., E. Iakovleva, D. Lesselier, and G. Perrusson, "MUSIC type electromagnetic imaging of a collection of small three-dimensional inclusions," *SIAM J. Sci. Comput.*, Vol. 29, 674–709, 2007.

18. Zhong, Y. and X. Chen, "MUSIC imaging and electromagnetic inverse scattering of multiply scattering small anisotropic spheres," *IEEE Trans. Antennas & Propag.*, Vol. 55, 3542–3549, 2007.

19. Chen, X. and K. Agarwal, "MUSIC algorithm for two-dimensional inverse problems with special characteristics of cylinders," *IEEE Trans. Antennas & Propag.*, Vol. 56, 1808–1812, 2008.

20. Odendaal, J. W., E. Barnard, and C. W. I. Pistorius, "Two dimensional superresolution radar imaging using the MUSIC algorithm," *IEEE Trans. Antennas & Propag.*, Vol. 42, No. 10, 1386–1391, 1994.

21. Yoon, Y. S. and M. G. Amin, "High-resolution trough-the-wall radar imaging using beamspace MUSIC," *IEEE Trans. Antennas & Propag.*, Vol. 56, 1763–1774, 2008.

22. Chew, W. C., *Waves and Fields in Inhomogeneous Media*, 2nd edition, IEEE Press, New-York, 1995.

23. Xiao, S.-Q., J. Chen, X.-F. Liu, and B.-Z. Wang, "Spatial focusing characteristics of time reversal UWB pulse transmission with different antenna arrays," *Progress In Electromagnetics Research B*, Vol. 2, 223–232, 2008.

24. Yu, G. and T.-J. Cui, "Imaging and localization properties of LHM superlens excited by 3D horizontal electric dipoles," *Journal of Electromagnetic Waves and Applications*, Vol. 21, No. 1, 35–46, 2007.